

Magic Angle Spinning NMR Structure Determination of Proteins from Pseudocontact Shifts

Jianping Li,[†] Kala Bharath Pilla,[§] Qingfeng Li,[‡] Zhengfeng Zhang,[†] Xuncheng Su,[‡] Thomas Huber,[§] and Jun Yang^{*,†}

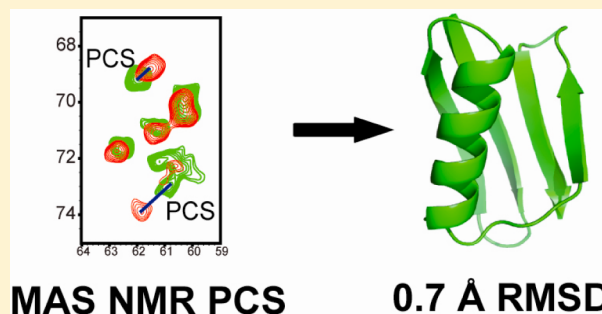
[†]Key Laboratory of Magnetic Resonance in Biological Systems, State Key Laboratory of Magnetic Resonance and Atomic and Molecular Physics, Wuhan Centre for Magnetic Resonance, Wuhan Institute of Physics and Mathematics, Chinese Academy of Sciences, Wuhan, 430071, PR China

[‡]State Key Laboratory of Elemento-Organic Chemistry, Nankai University, Tianjin 300071, PR China

[§]Research School of Chemistry, Australian National University, Canberra, ACT 0200, Australia

S Supporting Information

ABSTRACT: Magic angle spinning solid-state NMR is a unique technique to study atomic-resolution structure of biomacromolecules which resist crystallization or are too large to study by solution NMR techniques. However, difficulties in obtaining sufficient number of long-range distance restraints using dipolar coupling based spectra hamper the process of structure determination of proteins in solid-state NMR. In this study it is shown that high-resolution structure of proteins in solid phase can be determined without the use of traditional dipolar–dipolar coupling based distance restraints by combining the measurements of pseudocontact shifts (PCSs) with Rosetta calculations. The PCSs were generated by chelating exogenous paramagnetic metal ions to a tag 4-mercaptomethyl-dipicolinic acid, which is covalently attached to different residue sites in a 56-residue immunoglobulin-binding domain of protein G (GB1). The long-range structural restraints with metal–nucleus distance of up to ~20 Å are quantitatively extracted from experimentally observed PCSs, and these are in good agreement with the distances back-calculated using an X-ray structure model. Moreover, we demonstrate that using several paramagnetic ions with varied paramagnetic susceptibilities as well as the introduction of paramagnetic labels at different sites can dramatically increase the number of long-range restraints and cover different regions of the protein. The structure generated from solid-state NMR PCSs restraints combined with Rosetta calculations has 0.7 Å root-mean-square deviation relative to X-ray structure.



INTRODUCTION

Magic angle spinning (MAS) solid-state NMR has emerged as a unique spectroscopic tool to elucidate the structure and dynamics of the challenging biological macromolecules,^{1–3} such as membrane proteins and proteins that are not amenable to either X-ray crystallography or solution NMR spectroscopy. In the past decade, with the availability of high magnetic fields up to ~21.1 T, high-performance MAS NMR probes, multidimensional radio frequency (RF) pulse sequences, novel techniques of isotopic labeling, and sample preparation, MAS NMR has made great progress in structure determination of the proteins, leading to the generation of atomic-resolution 3D structure of proteins with the size up to ~20 kDa.^{4–19} Although MAS NMR is in principle able to structurally characterize large proteins like typical seven-helix trans-membrane G protein-coupled receptors (GPCR) in the lipid bilayers,^{20–22} the application of the method for structure determination is not yet routine. One of the major bottlenecks is obtaining sufficient number of unambiguous long-range distance restraints for 3D structural characterization. Almost all

MAS NMR 3D structures of proteins reported to date were determined using distance restraints based on through-space dipole–dipole couplings between ¹H, ¹³C, and ¹⁵N nuclei and recorded in 2D or 3D correlation experiments, such as PDSD²³/DARR,²⁴ CHHC/NHHC,²⁵ TEDOR,^{26,27} and PAINCP/PAR.²⁸ Dipolar interaction in the solid state quickly leads to multistep magnetization transfer, rendering assignment and distance measurement more challenging. The difficulties in obtaining restraints corresponding to distance >5 Å by these methods arise from the weak dipole–dipole couplings between ¹H, ¹³C, and ¹⁵N, which are proportional to nuclear gyromagnetic ratios of those spins and also to the inverse third power of the nucleus–nucleus distance. However, restraints corresponding to long distance (>5 Å) are crucially important in defining the global protein folding, especially for multiple domains or large-size proteins. To overcome these limitations requires development of new techniques.

Received: February 27, 2013

Published: May 6, 2013

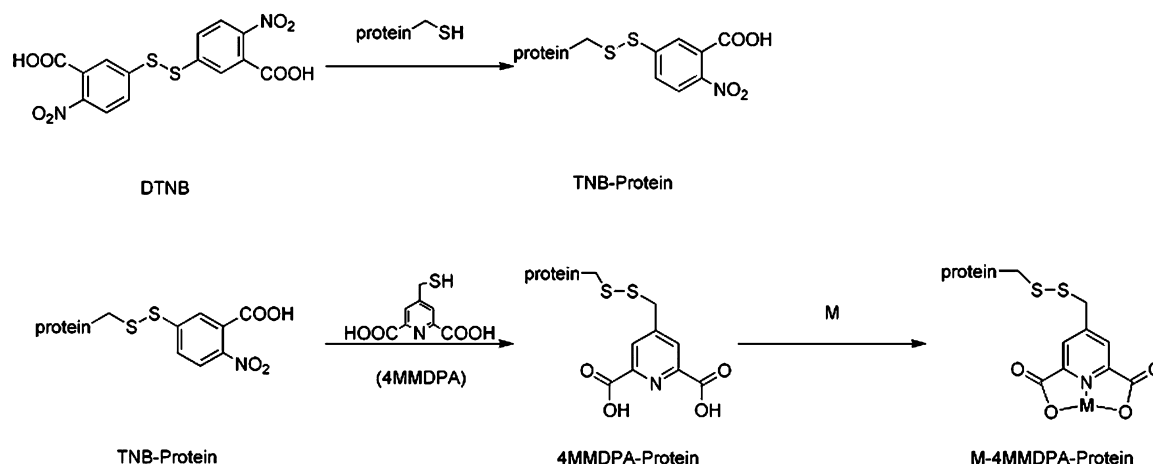


Figure 1. Ligation of 4MMDPA to cysteine mutants protein and binding of metal ions to 4MMDPA-protein ($M = \text{Co}^{2+}$, Zn^{2+} , Yb^{3+} , Tm^{3+} , or Lu^{3+}).

The electron–nucleus hyperfine couplings produce longer range distance restraints because the electron gyromagnetic ratio is 2–3 orders of magnitude larger than nuclear gyromagnetic ratio, and the structural restraints from paramagnetic center have been widely used in structure determination of proteins in solution NMR.^{29,30} Among paramagnetic restraints, pseudocontact shifts (PCS) can potentially be an informative probe. PCS is a chemical shift change due to anisotropic susceptibility of the paramagnetic center.³¹ It depends on the distance between nucleus and electron as well as orientations of metal–nucleus vector with respect to the principal axes of the χ tensor

$$\Delta\delta^{\text{PCS}} = \frac{1}{12\pi} \left[\Delta\chi_{\text{ax}} \frac{3\cos^2\theta - 1}{r^3} + \frac{3}{2} \Delta\chi_{\text{rh}} \frac{\sin^2\theta \cos 2\varphi}{r^3} \right]$$

Where $\Delta\chi_{\text{ax}}$ and $\Delta\chi_{\text{rh}}$ are the axial and rhombic components of the magnetic susceptibility anisotropies; r is the distance between the unpaired electron and nucleus; θ and φ are polar angles of the metal–nucleus vector with respect to the principal axes of the χ tensor. During the past several years, a number of MAS NMR studies of $\text{U-}^{13}\text{C}$, ^{15}N enriched proteins containing paramagnetic ions have been reported.^{18,32–51} In recent studies of metalloprotein catalytic domain of matrix metalloproteinase 12 (CoMMP-12)^{36,42} and Co^{2+} -substituted superoxide dismutase (Co^{2+} -SOD),^{18,47} PCSs were observed to significantly improve the resolution of protein structure calculated with solid-state NMR spectroscopy.

In this study, we present high-resolution structure determination of a protein from PCSs measured by solid-state NMR spectroscopy without the use of any other restraints. PCSs were generated by chelating exogenous paramagnetic metal ions to a tag 4-mercaptomethyl-dipicolinic acid (4MMDPA),⁵² which is covalently attached to different residue sites in a 56-residue GB1 protein, used by us as a model system.⁵³ By using multiple paramagnetic metal ions and multiple tagging sites, we observed a large number of PCSs covering comprehensively the protein's structure. High-resolution 3D structure (0.7 Å RMSD relative to X-ray structure) was calculated using experimentally measured PCSs combined with the Rosetta method.^{54–56}

EXPERIMENTAL SECTION

Protein Expression and Purification. Three single cysteine mutants K28C, D40C, and E42C of GB1 were constructed using

quick-change site-directed mutagenesis. The wild-type (wt) and mutant GB1 plasmids were introduced into a pET22b(+) vector. Proteins were expressed in *E. coli* BL21(DE3) in minimal medium containing 1 g/L NH_4Cl and 2 g/L glucose for natural abundance proteins or 1 g/L $^{15}\text{NH}_4\text{Cl}$ and 2 g/L ^{13}C -glucose for $\text{U-}^{13}\text{C}$, ^{15}N -enriched proteins. The cell suspension was incubated in water for 6 min at 80 °C for disrupting the cells and denaturing all nonthermostable proteins. After the initial purification step, the proteins ran over a HiTrap DEAE FF column as the final purification step. The proteins purity as well as the degree of isotopic label incorporation was checked by tricine-SDS-PAGE, microTOF mass spectrometry and solution-state NMR spectroscopy.

Ligation of 4MMDPA to the Mutant GB1. The reaction pathway for ligating 4MMDPA to GB1 mutants is shown in Figure 1. Since the three mutants have the same reaction path with the 4MMDPA, we only described the preparation of K28C-4MMDPA-GB1. All reaction steps were performed at room temperature. K28C-GB1 protein dissolved in 50 mM Tris-Cl pH 8.0 buffer was first reduced by 5 equiv of DTT and then concentrated to about 2.5 mM using a Millipore ultrafilter-15 with a MW cutoff of 3 kDa. Free DTT was removed by HiPrep 26/10 Dealtung, and the protein was eluted into 50 mM Tris-Cl at pH 7.6 (reaction buffer). Immediately thereafter, the protein was added stepwise into the 40 equiv of 5,5'-dithiobis-(2-nitrobenzoic acid) (DTNB) solution (4 mM, dissolved in the 50 mM Tris-Cl at pH 7.2), and the solution was mixed well after each addition. Reaction of protein and DTNB was performed at room temperature for 1 h, and the yellow thionitrobenzoate was generated during the reaction. Subsequently, excess DTNB and thionitrobenzoate was removed by a series of HiPrep 26/10 Dealtung, and protein was eluted into the reaction buffer. The activated protein was concentrated to about 2 mM. A 3-fold molar excess of 4MMDPA (in reaction buffer) was added to the activated protein solution. The reaction solution was left at room temperature for 2 h and subsequently desalted into reaction buffer. Finally, the product was purified using a MonoQ 5/50 GL column. The incorporation of 4MMDPA into K28C-GB1 was confirmed by microTOF mass spectrometry and solution-state NMR.

Solution NMR Spectroscopy. Paramagnetic metal ions (Co^{2+} , Yb^{3+} and Tm^{3+}) as well as diamagnetic metal ions (Zn^{2+} and Lu^{3+}) were titrated into the K28C-4MMDPA-GB1 solution during the solution NMR. For simplicity, we refer to the Co^{2+} loaded K28C-4MMDPA-GB1 complex as Co28-4MMDPA. Samples for solution NMR consisted of 2 mM ^{15}N K28C-4MMDPA-GB1 in 50 mM sodium phosphate H_2O buffer (for Co^{2+} and Zn^{2+}) at pH 5.5 or in 20 mM Hepes H_2O buffer (for Yb^{3+} , Tm^{3+} , and Lu^{3+}) at pH 7.5 and 10% D_2O in a total volume of 550 μL , respectively. 2D and 3D solution NMR experiments were performed at 25 °C on a Bruker DMX 600 MHz spectrometer equipped with a triple resonance TXI S3 XYZ gradient probe.

Preparation of Microcrystalline Protein Samples. In order to minimize the contribution of the intermolecular PCSs, paramagnetic and diamagnetic U- ^{13}C , ^{15}N enriched proteins were diluted by the natural abundance (na) wt GB1 in the molar ratios of 1:4 or 1:8, which were determined by both the resolution and signal-to-noise ratio of the corresponding MAS NMR spectra. To get a good-quality microcrystalline sample that would yield high-resolution solid-state NMR spectra, we screened conditions for cocrystallization of paramagnetically labeled and na-wt-GB1. Using slow dialysis for more even mixing of buffer solution with protein, we get robust crystallization conditions for proteins loaded with different metal ions.

All the microcrystalline protein samples were obtained by dialysis using a dialysis bag with a MW cutoff of 1 kDa. Solution of na-wt-GB1 and ^{13}C , ^{15}N -M28-4MMDPA ($M = \text{Co}^{2+}$, Zn^{2+} , Yb^{3+} , Tm^{3+} , or Lu^{3+}) was separately concentrated to 5 mg/mL in 50 mM sodium phosphate pH 5.5 buffer (for U- ^{13}C , ^{15}N -Co/Zn28-4MMDPA) or in 20 mM Hepes pH 7.5 buffer (for ^{13}C , ^{15}N -28Lu/Yb/Tm-4MMDPA). Immediately thereafter, two protein solutions were mixed well in the dialysis bag in the molar ratio of 1:4 (for ^{13}C , ^{15}N Co/Zn/Yb28-4MMDPA:na-wt-GB1) or 1:8 (^{13}C , ^{15}N -Tm28-4MMDPA:na-wt-GB1). The mixtures in the dialysis bag are dialyzed statically at 4 °C for 76 h in the precipitant solution containing 2-methyl-2,4-pentanediol, isopropyl alcohol, and deionized water in the volume ratio of 2:1:1.⁵³ Finally, the resulting microcrystalline protein samples were centrifuged at 18 000 g and transferred into 4 mm Varian standard-wall zirconia rotors.

Solid-State NMR Spectroscopy. All MAS NMR experiments were performed on a wide-bore Varian 600 MHz VNMRS NMR spectrometer, equipped with a 4 mm triple-resonance T3-HXY MAS probe, at a temperature of 283 K (calibrated in separate experiments using the lead nitrate temperature standard).⁵⁷ The sample spinning frequency was set to $11\,111 \pm 2$ Hz. The chemical shifts were referenced with respect to adamantane used as external referencing standards (40.48 ppm for the downfield carbon).⁵⁸ For most of the experiments, the pulse lengths were 3.3 μs (^1H), 4.3 μs (^{13}C), and 5.9 μs (^{15}N). The ^1H -X ($X = ^{15}\text{N}$ or ^{13}C) cross-polarization employed ~ 50 kHz ^1H RF field with linear amplitude ramp (90–110%), and the heteronucleus matched to the first Hartmann–Hahn condition. The band-selective magnetization transfer from ^{15}N to ^{13}C was realized using 5 ms SPECIFIC-CP⁵⁹ with tangent amplitude ramp and 7, 4, and 83 kHz RF power on ^{15}N , ^{13}C , and ^1H , respectively. The ^1H decoupling power of ~ 70 kHz was typically used during the acquisition and evolution periods in the 2D experiments. All spectra were processed in NMRpipe⁶⁰ and analyzed in Sparky.

Structure Calculations for GB1 using MAS NMR PCSs. PCSs were measured using cobalt metal ion (Co^{2+}) bound to the 4MMDPA tag, and a total of 79, 71, and 94 PCSs of the protein backbone atom nuclei of the mutants K28C, D40C and E42C were used in the PCS-Rosetta calculations. For structure calculations a nonhomologous fragment library was generated using the amino acid sequence of GB1. Three independent simulations were carried out generating around 5000 backbone-only models in a PCS-Rosetta low-resolution phase for each of the mutants. The relative weighting factor for the PCS score to the Rosetta's low-resolution energy function was computed as described in ref 55 and found to be 70.8, 90.1, and 46.0 for the mutants K28C, D40C, and E42C. Using a low PCS and centroid score cutoff of 65 and 20 for mutants K28C and D40C and 45 and 20 for mutant E42C, a subset of models was chosen for computationally expensive Rosetta's all-atom refinement. For each backbone-only model, 10 independent all-atom refinements were carried out, generating 10 times more structures than initial models. The final selection of structures is based on a combined score of Rosetta and PCS energy. To sample realistic metal positions during the fitting of PCS data for the scoring of the all-atom refined structures, a 3D spherical grid search for metal positions is carried out, where the radius of the sphere is chosen as 13 Å from the C_β of the mutant site which is chosen as the center of the sphere with grid step size of 0.5 Å. The radius of the sphere was calculated based on a rotamer library generated using the 3D structure of 4MMDPA. The results were compared to the crystal structure of the GB1 (PDB ID: 1PGA).

RESULTS AND DISCUSSION

Solution NMR Characterization of Metal-4MMDPA-GB1 Complex. Prior to PCS measurements, we performed a series of experiments to characterize the metal-4MMDPA-GB1 complex using solution NMR. First, we conducted titration experiments of Co^{2+} to GB1 mutants with and without 4MMDPA attachment, respectively, by monitoring the corresponding ^1H - ^{15}N HSQC spectra of U- ^{15}N labeled protein. With addition of Co^{2+} to the solution of diamagnetic GB1 mutants to progressively increase ion:protein molar ratio up to 1.1:1, no obvious chemical shift perturbations were observed in the spectra, indicating no specific interactions between Co^{2+} and GB1 mutants. In contrast, addition of Co^{2+} to the solution of GB1-4MMDPA construct resulted in appearance of new peaks corresponding to each backbone amides along with metal-free peaks. As the concentration of Co^{2+} was systematically increased, progressive enhancement of paramagnetic-shifted peaks was observed accompanied by the depression of metal-free cross peaks. Finally, the metal-free peaks were completely missing once excess of metal was added and the ion:protein molar ratio reached 1.1:1. Neither new peaks appeared nor additional paramagnetic-induced shifts were observed upon further addition of Co^{2+} to a final ion concentration of 3 fold excess with respect to the protein. The titration experiments indicate that the chelation of the residues by 4MMDPA tag gives rise to highly specific binding of metal ions to the corresponding sites. In addition, to evaluate the change of protein structure with the introduction of metal loaded 4MMDPA tag, we recorded ^1H - ^{15}N HSQC spectra of diamagnetic Zn-4MMDPA protein and compared those to the corresponding spectra of the wt-GB1. As the overwhelming majority of difference of chemical shifts between corresponding peaks in Zn42-4MMDPA GB1 and wt-GB1 spectra are within 0.1 ppm for $^1\text{H}^{\text{N}}$ and 0.5 ppm for $^{15}\text{N}^{\text{H}}$, respectively, we conclude that mutations followed by 4MMDPA attachment as well as metal ions binding do not significantly perturb the structure of wt-GB1 (Figure 2a and Figure S1).

Preparation of Paramagnetic Microcrystalline Protein Samples for Solid-State NMR. The focus of this study is to determine structure via the measurement of intramolecular PCSs. To observe pure intramolecular PCSs, the U- ^{13}C , ^{15}N labeled paramagnetic protein molecules must be diluted by natural abundance diamagnetic protein matrix to avoid intermolecular interaction. However, mixing of Co-4MMDPA (or Yb/Tm-4MMDPA) protein mutants and their diamagnetic counterpart Zn-4MMDPA (or Lu-4MMDPA) in solution required for the microcrystal formation suffers from the problem of rapid exchange of paramagnetic ions in U- ^{13}C , ^{15}N labeled protein and diamagnetic ions in natural abundance protein, resulting in undesirable diamagnetic U- ^{13}C , ^{15}N labeled and paramagnetic natural abundance proteins.³⁸ We observed by ^1H - ^{15}N HSQC spectra that 30 min of mixing of U- ^{13}C , ^{15}N labeled Co42-4MMDPA and na-Zn42-4MMDPA at a molar ratio of 1:4 results in an almost even distribution of Co^{2+} and Zn^{2+} in all protein molecules (enriched and not-enriched). The time for the full redistribution of Co^{2+} and Zn^{2+} between 4MMDPA binding sites is much shorter than that required for the microcrystal formation. To overcome this problem, in the subsequent sample preparations, we utilized wt-na-GB1 to dilute the paramagnetic U- ^{13}C , ^{15}N GB1 to prevent exchange of metal ions; there are not high affinity metal binding sites in wt-GB1.³⁸

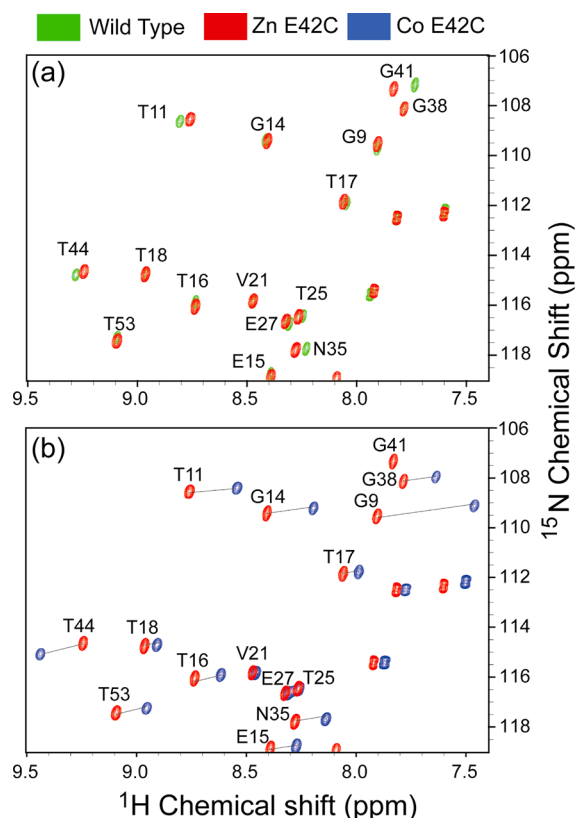


Figure 2. Region of 600 MHz $2\text{D } ^1\text{H}-^{15}\text{N}$ HSQC spectra of (a) Zn42-4MMDPA (red) and wt-GB1 (green) and (b) Zn42-4MMDPA (red) and Co42-4MMDPA GB1 (blue).

High-ratio dilution is favorable to obtain pure intramolecular PCSs and avoid intermolecular interaction. However, high-ratio dilution results in lower signal-to-noise ratio since the volume of a MAS rotor is limited, and hence a lower amount of $\text{U-}^{13}\text{C}, ^{15}\text{N}$ enriched proteins (the only species giving rise to the NMR signal) can be loaded in the MAS rotor. The practically attainable dilution ratio is thus a compromise between intramolecular PCSs measurement and acceptable sensitivity. We found that the resolution of MAS NMR spectra of paramagnetic proteins in this study is strongly dependent on the dilution ratio, and the insufficient dilution leads to poor resolution. With the systematic screening of the dilution ratio in proteins containing metal ions with different paramagnetic susceptibility, such as Co^{2+} and Yb^{3+} with medium paramagnetic susceptibility and Tm^{3+} with highly paramagnetic susceptibility, we found that higher dilution ratio is required for the proteins containing metal ions with highly paramagnetic susceptibility to obtain high-resolution MAS NMR spectra. For example, our experiments showed that 1:4 dilution ratio is sufficient to acquire high-resolution MAS NMR spectra containing pure intramolecular paramagnetic-shifted signals for Yb^{28} - and Co^{28} -4MMDPA. At the same time, 1:4 dilution ratio is not enough for Tm^{28} -4MMDPA under these conditions intermolecular interactions are still present. In Figure S2, we show 2D NCA MAS NMR spectra of $\text{U-}^{13}\text{C}, ^{15}\text{N}$ enriched of Tm^{28} -4MMDPA with 1:6 and 1:8 dilution ratio samples. In the spectra with 1:8 dilution, the resolution is remarkably improved than that in 1:6 spectra and allows for the majority of intramolecular paramagnetically shifted resonances to be assigned. Based on the results of this systematic screening of the dilution ratio, 1:4, 1:4, and 1:8 dilution ratios were finally

used for preparation of Co^{2+} , Yb^{3+} , Tm^{3+} -4MMDPA protein samples, respectively.

To obtain high-quality microcrystalline samples that yield high-resolution solid-state NMR spectra, we screened conditions for cocrystallization of paramagnetically labeled GB1 and na-wt-GB1. We found that the quality of crystalline of Tm and Yb loaded GB1 (diluted by na-GB1) is more sensitive to the crystallization conditions than that of Co complex. Using slow dialysis for more even mixing of buffer solution with protein, we get robust crystallization conditions for proteins loaded with different metal ions.

Solid-State NMR PCS Measurements and Fitting of $\Delta\chi$ Tensor Parameters. 2D MAS NMR spectra of $\text{U-}^{13}\text{C}, ^{15}\text{N}$ enriched Co42- and Zn42-4MMDPA (with dilution) are shown in Figure 3. Additional spectra of $\text{U-}^{13}\text{C}, ^{15}\text{N}$ enriched Tm- and Yb-4MMDPA GB1 samples are included in the Supporting Information. The inspection of the spectra reveals only minor paramagnetic relaxation enhancement (PRE) due to the

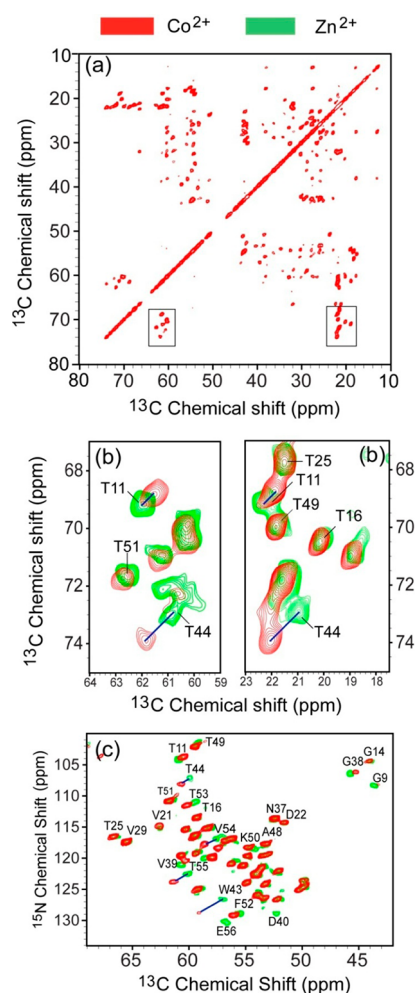


Figure 3. (a) 2D ^{13}C - ^{13}C MAS NMR spectra of Zn42-4MMDPA microcrystalline GB1 with 5 ms DARR mixing time. (b) Representative regions of 2D ^{13}C - ^{13}C DARR and (c) NCA MAS NMR spectra are superimposed for $\text{U-}^{13}\text{C}, ^{15}\text{N}$ enriched Co42-4MMDPA-GB1 (red) and Zn42-4MMDPA-GB1 sample (green). Blue lines indicate PCSs. In order to obtain pure intramolecular PCSs, both samples were prepared using ~ 5 mg $\text{U-}^{13}\text{C}, ^{15}\text{N}$ enriched Zn42 and Co42-4MMDPA GB1 molecules diluted by natural abundance wt-GB1 with molar ratio 1:4. Total measurement time of 2D DARR and NCA spectra is about 8 and 12 h, respectively.

paramagnetic Co^{2+} that manifests itself in line broadening of signals. The majority of the signals in the spectra of Co42–4MMDPA sample have very similar line width to those in the spectra of its (diamagnetic) Zn counterpart. Most importantly, only one paramagnetic species in the spectrum of Co42–4MMDPA was observed, suggesting pure intramolecular paramagnetic contribution and little influence of intermolecular interactions of neighboring protein molecules. The high quality of the spectra of paramagnetic protein allows most of the resonances to be assigned using $\text{U-}^{13}\text{C},^{15}\text{N}$ enriched samples and a set of 2D $^{13}\text{C-}^{13}\text{C}$ DARR, $^{15}\text{N-}^{13}\text{C}_\alpha$ (NCA), $^{15}\text{N-}^{13}\text{C}_\alpha$ - C_α (NCACX), $^{15}\text{N-}^{13}\text{C}'$ - C_α (NCOCX) experiments. With these spectra, we have assigned the majority of the resonances in paramagnetic and diamagnetic M28-, M40-, and M42-4MMDPA ($M = \text{Co}, \text{Zn}, \text{Lu}, \text{Yb}, \text{Tm}$). PCSs are measured as the chemical shift differences between paramagnetic proteins and their diamagnetic counterparts (Zn^{2+} and Lu^{3+} as a reference of Co^{2+} and $\text{Yb}^{3+}/\text{Tm}^{3+}$, respectively). To reduce the uncertainty of PCS measurements, chemical shifts were recorded in both paramagnetic and diamagnetic proteins using the averaged value of chemical shifts in two or more corresponding 2D spectra. The experimental and back-calculated PCSs of Co, Yb, and Tm ions ligated to different mutant sites are shown as a function of the residue number in Figure 4. The inspection of these plots reveals the apparent dependence of the magnitude of the PCSs on the distance between nuclei and paramagnetic metal ions. For example, the residues with the largest observed PCS of metal ions loaded at different mutant sites are all in the immediate proximity to the mutation sites in the structure model. To further compare the experimentally observed and back-calculated PCSs and extracted distances, Figure 5a,b displays the back-calculated and observed PCSs and distances, respectively. The X-ray structure model (PDB code 1PGA) of GB1 was used for the fitting of the $\Delta\chi$ parameters and back calculations from experimentally observed PCSs. With the assumption that the uncertainty of PCSs measurements in MAS NMR is ~ 0.1 ppm, the distances extracted from PCSs with $|\Delta\delta_{\text{PCS}}| < 0.2$ ppm will have large uncertainty. Only distances with corresponding PCS ($|\Delta\delta_{\text{PCS}}| > 0.2$ ppm) are presented in the plots. Figure 5 shows a good agreement between observed and back-calculated values, strongly suggesting that PCSs in solid-state NMR can be used as a source of long-range distance restraints for protein structure determination, just like in the solution NMR.

Comparison of PCSs in Solution NMR and in Solid-State NMR. To measure PCSs of Co42–4MMDPA in the solution, we collected a set of 2D and 3D chemical shift correlation spectra of paramagnetic proteins and their diamagnetic Zn^{2+} counterparts. The PCSs were measured as the chemical shift difference of paramagnetic (Co^{2+}) and diamagnetic proteins (Zn^{2+}). In Figure 2b, we show a small region where $^1\text{H-}^{15}\text{N}$ HSQC 2D spectrum of Co42-4MMDPA are superimposed. The resonances of these spectra were assigned based on HNCA and HNCACO 3D spectra of $\text{U-}^{13}\text{C},^{15}\text{N}$ enriched paramagnetic and diamagnetic proteins samples. PCS measurements of the same paramagnetic proteins in solution and in microcrystalline state allow comparison of the PCSs from solution and solid-state NMR. The PCSs of Co42-4MMDPA in solid-state and solution NMR as a function of the residue number are shown in Figure 6. The most striking difference between solution and solid-state PCSs of Co42-4MMDPA is that the sign of the PCSs is opposite, with positive sign in vast majority of PCSs in solid-state NMR and negative

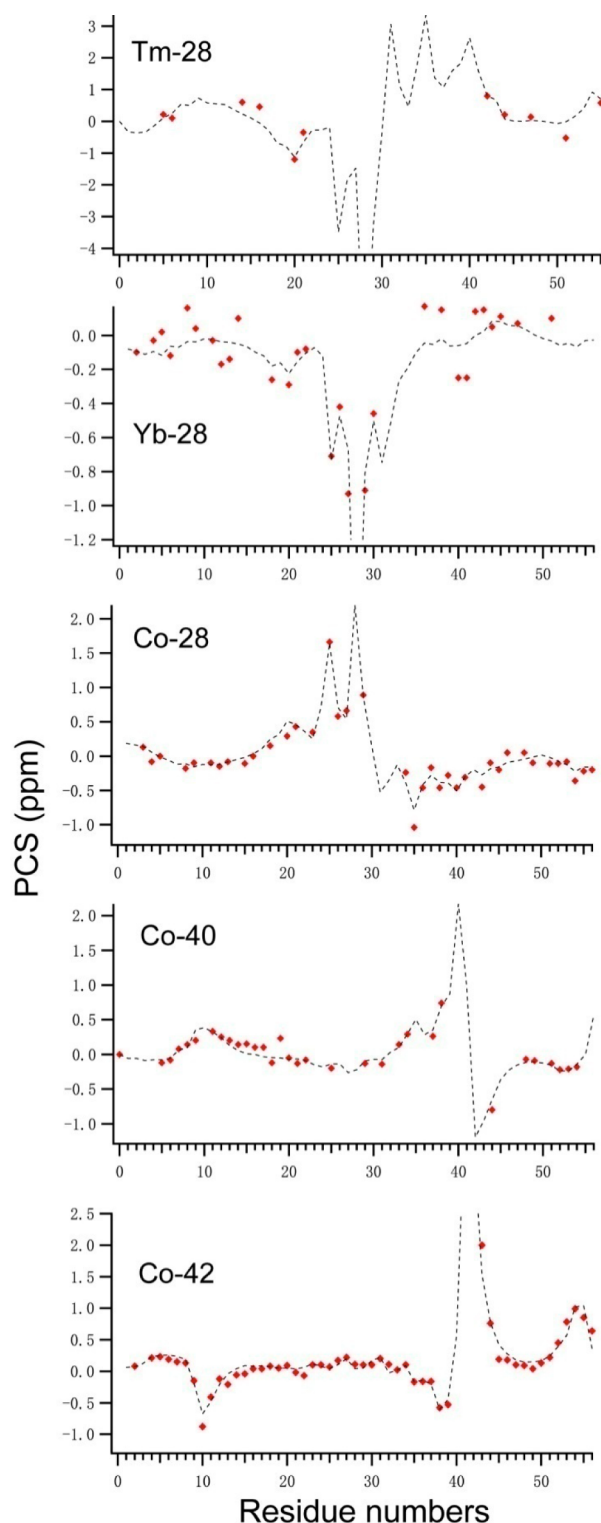


Figure 4. $^{13}\text{C}_\alpha$ observed (red solid dots) and back-calculated (dashed lines) MAS NMR PCSs plotted as a function of the residue number. The X-ray structure model (PDB ID: 1PGA) of GB1 was used for the fitting of the $\Delta\chi$ parameters and back calculations. It should be noted that although only C_α PCSs are plotted in this figure, the fittings of the $\Delta\chi$ tensor parameters use all ^{13}C and ^{15}N PCSs.

sign in almost all of PCSs of solution NMR, indicating a difference of the $\Delta\chi$ tensor orientation in the solid and solution state. Indeed, the fitting of experimentally measured PCSs in the two states shows the difference of three Euler angles as well

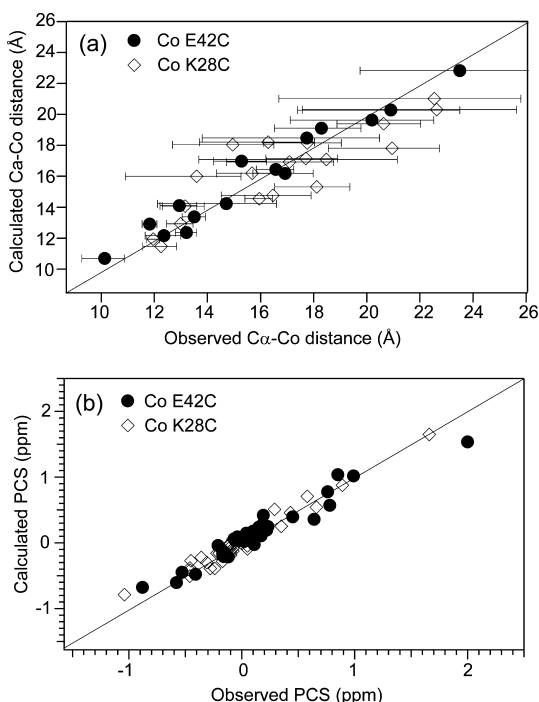


Figure 5. Comparison between the experimentally observed (a) $r_{\text{Ca-Co}}$ and (b) MAS NMR $^{13}\text{C}_\alpha$ PCSs, and the corresponding values derived from structural model of Co28- and Co42-4MMDPA GB1. The X-ray structure model (PDB ID: 1PGA) of GB1 was used for the fitting of the $\Delta\chi$ parameters and back calculations. The uncertainty of $r_{\text{Ca-Co}}$ was estimated by assuming the uncertainty of measurement of PCSs to be 0.1 ppm.

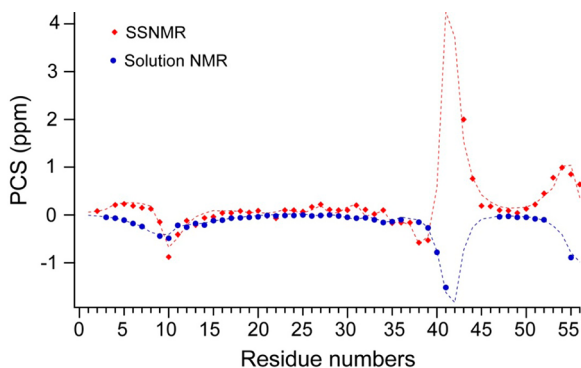


Figure 6. Experimental $^{13}\text{C}_\alpha$ (red, solid-state NMR) and $^1\text{H}_\beta$ (blue, solution NMR) and the corresponding back-calculated (dashed lines) PCSs are plotted as a function of residue number for Co42-4MMDPA-GB1.

as the magnitude of $\Delta\chi$ tensor. The metal ion coordination for Co42-4MMDPA in solid and solution state inferred from the fitting is not spatially similar. We also tried to fit solid (or solution) PCSs using restricted metal ion coordination (with 2 Å variation) determined from solution (or solid) PCSs. The resulting fits are of inferior quality. The least distance between Co^{2+} and atoms in residues on the surface of the protein is more than 5 Å in both solution and solid state, indicating that the paramagnetic tags extend outside the protein. The large difference of the chemical environments of the paramagnetic tags in the solution and the microcrystal state likely contributes to the difference of conformations of paramagnetic tags in the solution and solid state and difference of metal ion

coordinations and orientations. The magnitude of $\Delta\chi$ in the solid state ($7.1 \times 10^{-32} \text{ m}^3$) is greater than that in the solution state ($-4.6 \times 10^{-32} \text{ m}^3$) (Table 1), which is likely due to the mobility of the paramagnetic tag in the solution. The observed different $\Delta\chi_{\text{ax}}$ tensors in solid and solution state in this study is markedly different than in the case of CoMMP-12 by Bertini et al.,³⁶ in which they observed consistent PCSs in solid and solution state when the paramagnetic metal ions are in an internal, nonsolvent-exposed environment. Their observations reflect the similar local chemical environment around the paramagnetic metal ions in the solid and solution states. However, in this study, the paramagnetic tag bound to solvent-exposed cysteine residues, which allows the metal ion more sensitive to the local chemical environment in solution and solid state.

Solid-State NMR PCSs of Multiple Metal Ions and Multiple Binding Sites. The paramagnetic center in protein permits to highlight residues in spatial proximity to it and within which reliable PCS-based restraints can be extracted. The minimum and maximum distance to the paramagnetic center where residues can be seen and PCSs are detectable depends on the paramagnetic properties of metal ions. Residues in close proximity to the paramagnetic sites are not detectable by NMR because of the line broadening induced by PRE to the corresponding nuclei. Residues distal to the metal center possess too small PCSs to be detected. Additionally, there are also blind sites positioned at unfavorable angles (θ close to 54.7°).⁶¹ The above can be simplistically described as the PCS shell. The “dark” space in this shell undetectable by PCSs from one paramagnetic ion may exhibit distinct PCS from another metal ion with different paramagnetic susceptibility and thus with different tensor orientation and PCS field. Therefore, using metal ions with different paramagnetic susceptibility allows the tuning of the active area in which PCSs are structural informative on (fragments of) the protein. In Figure 4, the PCSs of Yb28-, Co28- and Tm28-4MMDPA are displayed as a function of the residue number. The number of observed PCSs of Tm28-4MMDPA is fewer than that of Co28- and Yb28-4MMDPA because of the high-dilution ratio in the former complex required to attain high-resolution of the solid-state NMR spectra in sample preparations and thus giving rise to low sensitivity, hampering assignments of some resonances. Compared to PCSs generated by Co^{2+} and Tm^{3+} , the PCSs generated by Yb^{3+} are relatively small and more than half of the PCSs are within 0.2 ppm. The parameters of $\Delta\chi$ tensor fitted from PCSs are listed in Table 1. The amplitudes of $\Delta\chi_{\text{ax}}$ of Co^{2+} ($8.5 \times 10^{-32} \text{ m}^3$) and Tm^{3+} ($-22.5 \times 10^{-32} \text{ m}^3$) are comparable to those in the literature, $7 \times 10^{-32} \text{ m}^3$ for Co^{2+} and $26 \times 10^{-32} \text{ m}^3$ for Tm^{3+} ,⁶² respectively. However, the amplitude of $\Delta\chi_{\text{ax}}$ of Yb^{3+} ($2.9 \times 10^{-32} \text{ m}^3$) is much smaller than that reported in the literature⁶² ($8.5 \times 10^{-32} \text{ m}^3$). The orientations of $\Delta\chi$ of these metal ions are different, as expected. As an example, the “lit up” shells of Co28- and Tm28-4MMDPA are shown in Figure 7. Tm^{3+} , with its $\Delta\chi_{\text{ax}}$ magnitude being 2–3 fold greater than that in Co^{2+} , generates the PCSs active shell of larger thickness. In Figure 7, we show the back-calculated distance between nucleus to metal with $|\Delta\delta_{\text{PCS}}| > 0.2 \text{ ppm}$, plotted onto the GB1 ribbon diagram. The residues in $\beta 1$ and $\beta 2$ strands inaccessible by Co^{2+} , due to large distances and unfavorable angles, can be covered by Tm^{3+} PCSs, where PCSs at the distances between nucleus and metal up to 25 Å can be detected.

Table 1. Comparison of $\Delta\chi$ Tensors in GB1 Ligated with 4MMDPA from Solution and Solid State NMR PCS and Using Crystal and PCS Rosetta Calculated Structures

mutant	metal ion	structure	$\Delta\chi_{ax}$	$\Delta\chi_{rh}$	x	y	z	α	β	γ
K28C	Co ²⁺	crystal ^a	8.5(0.1)	3.4(0.1)	15.946	34.498	16.721	32	60	48
K28C	Co ²⁺	PCS-Rosetta ^b	7.0(0.2)	3.3(0.2)	16.119	34.372	18.132	29	66	43
D40C	Co ²⁺	crystal ^a	7.4(0.1)	1.9(0.1)	13.182	22.638	12.359	156	77	59
D40C	Co ²⁺	PCS-Rosetta ^b	6.2(0.2)	1.2(0.2)	13.719	22.824	13.671	160	73	39
E42C	Co ²⁺	crystal ^a	7.1(0.1)	3.5(0.1)	17.802	19.467	10.222	40	169	3
E42C	Co ²⁺	PCS Rosetta ^b	6.0(1.9)	3.2(1.2)	17.497	19.152	11.193	66	170	20
K28C	Yb ³⁺	crystal ^a	2.9(0.2)	1.5(0.1)	16.946	34.498	17.721	24	141	110
K28C	Tm ³⁺	crystal ^a	-22.5(0.5)	-15.0(0.4)	16.946	34.498	17.721	28	77	32
E42C ^c	Co ²⁺	crystal ^a	-4.6(0.1)	-1.4(0.1)	13.302	19.697	10.722	147	130	77

^aPCS are fitted to the crystal structure of GB1 [PDB ID: 1PGA]. ^bPCS are fitted to the final selected structure from the PCS-Rosetta calculation. ^cPCS data from solution NMR. The program Numbat⁶⁴ was used to fit the $\Delta\chi$ -tensors; axial and rhombic components (10^{-32} m³), the coordinates of paramagnetic ions (Å), and the Euler rotation angles (in degrees) are in the reference frame of the crystal structure 1PGA. The metal coordinates were fixed during tensor calculation and were determined by using a 3D spherical grid function which samples realistic metal positions.⁵⁵ Error estimates of the axial and rhombic components are given in brackets in the table and tensor rotation angles variation are shown as Sanson–Flansted projections in Figure S5. The error estimates were obtained by the Monte Carlo sampling using 1000 partial PCS data sets in which 10% of the input data were randomly removed, while retaining the metal position.

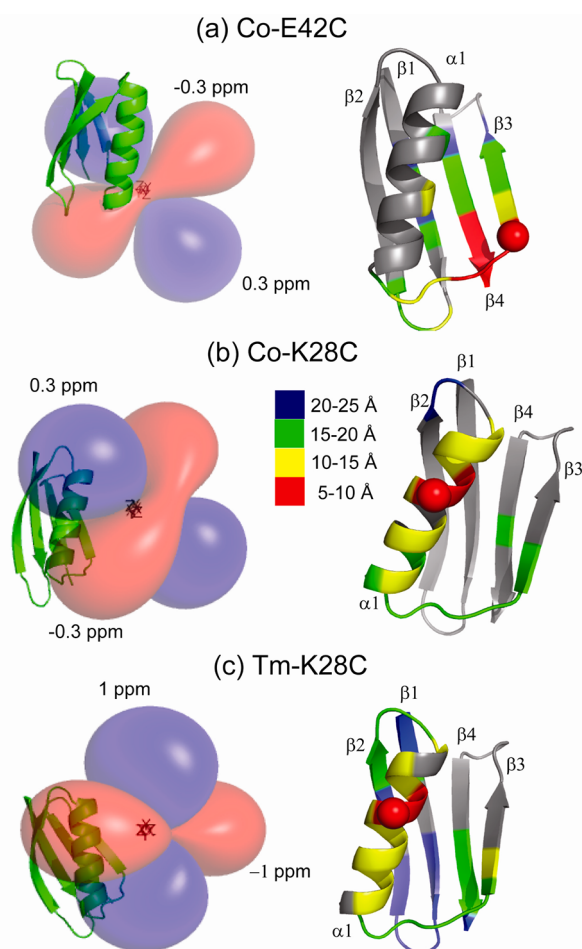


Figure 7. Isosurfaces of the PCS and ribbon diagram of (a) Co42-, (b) Co28-, and (c) Tm28-4MMDPA GB1. The isosurfaces were calculated for PCSs of ± 0.3 , ± 0.3 , and ± 1 ppm for (a–c), respectively. Blue and red surfaces identify positive and negative PCSs, respectively. Residues with $|\Delta\delta_{PCS}| > 0.2$ ppm and back-calculated $r_{Ca-Co} < 10$ Å, 10 Å $< r_{Ca-Co} < 15$ Å, 15 Å $< r_{Ca-Co} < 20$ Å, $r_{Ca-Co} > 25$ Å are shown in red, yellow, green, and blue, respectively. Residues with $|\Delta\delta_{PCS}| < 0.2$ ppm are displayed in gray.

Figure 7 illustrates that residues that experience very small or no PCS effect from one paramagnetic center often have appreciable PCS when the protein was tagged at other sites. In Figure 7 we compare the PCSs covered fragments of Co28- and Co42-4MMDPA. The residues in $\beta 2$ strand, not detectable by Co42-4MMDPA PCSs, can be accessible by Co28-4MMDPA PCSs. In addition, the “dark” area of $\beta 1$ strand, the loop between $\beta 1$ and $\beta 2$ strands of Co28-4MMDPA PCSs, can be covered by Co42-4MMDPA PCSs.

High-Resolution Structure Determination by PCS-Rosetta. Using PCS-Rosetta and in turn PCS data from a single metal center during folding, around 4500, 10 000, and 8400 all-atom models were generated for each of the mutants K28C, D40C, and E42C. To take the advantage of all three data sets for GB1, Rosetta’s all-atom structures for each of the mutants were rescored, and the final structures were selected based on low Rosetta energy and combined low PCS score from all three data sets. The energy profile of the folding simulation for each of the mutants is funneled toward the native-like structures (Figure 8a), and selected structures in each of the simulations resemble the structure determined by X-ray crystallography, with C_α RMSD < 1.2 Å and the lowest combined energy structure being 0.7 Å (Figure 8b). The tensor parameters for the lowest combined energy structure are represented in Table 1. The magnitude of axial and rhombic components of the tensor is found to be consistent for all the metal positions with low standard deviations, and $\Delta\chi$ tensors are very similar to the ones fitted to the crystal structure of GB1 (Table 1) resulting in nearly identical PCS isosurfaces (Figure S6). PCS-Rosetta was previously applied to accurately calculate 3D protein structures from high-quality PCS data, and it was demonstrated that the sampling efficiency of the native-like structures is greatly improved over equivalent CS-Rosetta calculations.⁵⁶ Using less accurate PCS data from solid-state NMR, we observed that incorporation of PCS restraints during Rosetta folding simulation did not improve the sampling of near-native structures when compared with sampling of unrestrained Rosetta folding simulation. However, the PCS information made it possible to select for native-like structures by screening for structures that satisfy multiple tensor fits in combination with low Rosetta energy. The selection is a highly significant advantage of the approach, because the accurate

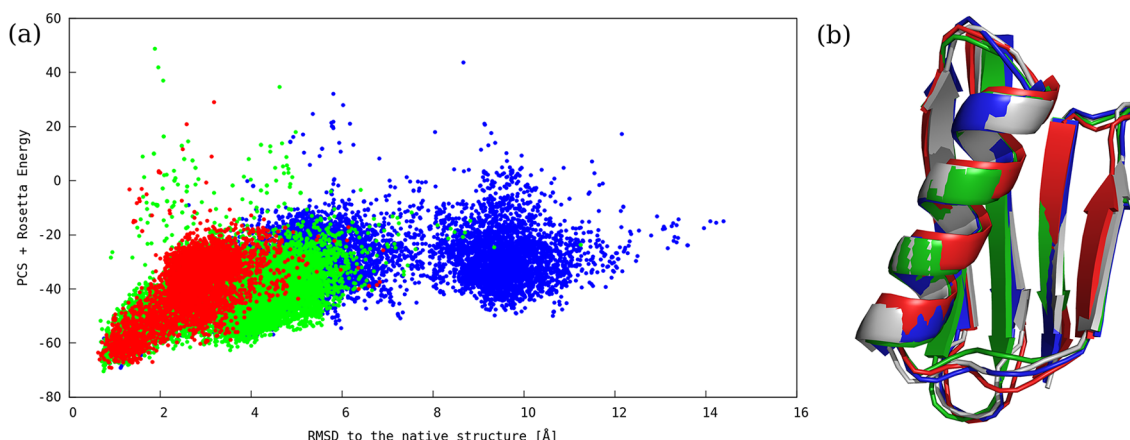


Figure 8. High-resolution structure calculation from solid-state NMR PCS using PCS-Rosetta. (a) Combined score of PCS energy from three tags and Rosetta energy versus the RMSD to the crystal structure of GB1 (PDB ID: 1PGA). Sampling from mutant K28C is represented in red color, D40C is represented in green color, and E42C is represented in blue color. The models with lowest combined score found have RMSD to the crystal structure as 0.9, 0.7, and 1.1 Å for mutants K28C, D40C, and E42C, respectively. (b) 3D representation of calculated models using PCS-Rosetta. The crystal structure of GB1 is represented in gray color, mutant K28C is represented in red color, D40C is represented in green color, and E42C is represented in blue color.

selection of near-native structures from a large number of well-formed decoys represents the most pressing challenge in structure determination from sparse experimental data. A structure determination procedure is consequently unsuccessful if it can produce a close-native structure but is unable to recognize it as such. PCS-Rosetta employs long-range PCS restraints to funnel the folding energy landscape from as far as 10 Å RMSD toward the native structure. In addition, the long-range PCS restraints are exceptionally well suited to discriminate alternative low-energy structures of incorrect folds.

MAS NMR High-Resolution Structure Determination of Proteins from PCS. The difficulties of the currently used dipolar-coupling-based spectra for long-range restraints assignment are related to high congestion of the spectra containing tens and hundreds or even thousands of cross peaks, and among these most peaks are associated with intraresidue or sequential-residue correlations. This congestion of the spectra is more severe for membrane proteins due to poor dispersion of chemical shifts and for large proteins with large number of backbone and side chain NMR signals. Moreover, the peaks arising from long-range correlations in the dipolar coupling based spectra usually possess low signal-to-noise ratio, making the MAS NMR experiments time-consuming with experimental time of 2D spectra as long as several days.^{10,63} These limitations can be addressed by using PCS-based approach. The most remarkable advantage of PCS-based approach is that it is easy and fast to obtain a large number of PCSs with high accuracy, simply by measuring the chemical shift difference between paramagnetic and diamagnetic species. Moreover, due to the intrinsically long distance nature of PCSs, the sensitivity of the PCS-based measurements is much higher compared with the dipolar coupling based techniques. These advantageous properties of PCS-based approach are expected to accelerate the structure determination of the proteins by solid-state NMR. Indeed, previous studies of PCSs in a metalloprotein³⁶ have shown great potential of PCSs as a source of long-range restraints for structure determination by solid-state NMR.

The focus of this work is to determine high-resolution structure of diamagnetic proteins by using restraints from PCSs combined with Rosetta calculations, without the use of traditional dipolar–dipolar coupling based distance restraints.

The PCS-Rosetta algorithm determines *ab initio* both $\Delta\chi$ tensor and 3D structure of a protein using only the primary amino acid sequence and the PCS data as input; it does not rely on any $\Delta\chi$ tensor parameters nor on the structure (or model) of the target protein. This is particularly beneficial for solid-state NMR because of the limitation of the currently used distance restraints from dipolar coupling based spectra. The most striking advantage of the artificially introduced paramagnetic ion is the flexibility to attach it to different solvent-exposed residue sites and generate PCSs from residues located on different fragments of the protein, as showed in Figure 7. Use of PCSs from the multiple binding sites of paramagnetic metal ions has been demonstrated to be important for the high-resolution structure determination in the Rosetta calculations. The approach of combining of paramagnetic tagging, spin dilution, PCS measurements and Rosetta calculations can be a general solid-state NMR route for high-resolution structure determination of proteins and widely applied to structural studies of membrane proteins and amyloid fibrils.

CONCLUSIONS

In summary, we have shown that high-resolution structure of diamagnetic proteins in solid phase can be generated from a combination of MAS NMR PCS measurements and Rosetta calculations. 2D high-resolution solid-state MAS NMR spectra of U-¹³C,¹⁵N enriched model protein GB1 containing covalently paramagnetic tags provide long-range structural restraints of 10–20 Å which are inaccessible to a dipolar coupling based approach. We also have shown the flexibility of introduction of different paramagnetic ions to different sites of the protein, enabling the coverage of several fragments of the protein and yielding more complete PCS-derived distance maps. The work reported here indicates that using PCSs as a source of long-range restraints can be a general route to structure determination of challenging biomacromolecules, such as membrane proteins and amyloid fibrils by solid-state NMR.

■ ASSOCIATED CONTENT

■ Supporting Information

Tables with solid-state NMR and solution NMR PCSs, and figures displaying solution NMR and MAS NMR spectra, and a figure showing uncertainty of $\Delta\chi$ tensor rotation angles. This material is available free of charge via the Internet at <http://pubs.acs.org>.

■ AUTHOR INFORMATION

Corresponding Author

yangjun@wipm.ac.cn

Notes

The authors declare no competing financial interest.

■ ACKNOWLEDGMENTS

J.Y. thanks Tatyana Polenova for valuable discussions. The authors thank Xu Zhang for help in solution NMR experiments. This work is supported by grants from the National Natural Science Foundation of China (21075133, 21173259, 21073101) and the National Basic Research Program of China (2009CB918600). We are thankful to King Abdulla University of Science and Technology (KAUST), Saudi Arabia, for providing access to the Blue Gene/P (Shaheen) supercomputer. T.H. acknowledges funding from the Australian Research Council, including a Future Fellowship (FT0991709) and project grant (DP120100561).

■ REFERENCES

- (1) Hong, M.; Zhang, Y.; Hu, F. H. *Annu. Rev. Phys. Chem.* **2012**, *63*, 1–24.
- (2) McDermott, A. *Annu. Rev. Biophys.* **2009**, *38*, 385–403.
- (3) Tycko, R. *Annu. Rev. Phys. Chem.* **2011**, *62*, 279–299.
- (4) Castellani, F.; van Rossum, B.; Diehl, A.; Schubert, M.; Rehbein, K.; Oschkinat, H. *Nature* **2002**, *420*, 98–102.
- (5) Zech, S. G.; Wand, A. J.; McDermott, A. E. *J. Am. Chem. Soc.* **2005**, *127*, 8618–8626.
- (6) De Paepe, G.; Lewandowski, J. R.; Loquet, A.; Bockmann, A.; Griffin, R. G. *J. Chem. Phys.* **2008**, *129*, 245201–245211.
- (7) Korukottu, J.; Schneider, R.; Vijayan, V.; Lange, A.; Pongs, O.; Becker, S.; Baldus, M.; Zweckstetter, M. *PLoS One* **2008**, *3*, 2359.
- (8) Loquet, A.; Bardiaux, B.; Gardiennet, C.; Blanchet, C.; Baldus, M.; Nilges, M.; Malliavin, T.; Bockmann, A. *J. Am. Chem. Soc.* **2008**, *130*, 3579–3589.
- (9) Manolikas, T.; Herrmann, T.; Meier, B. H. *J. Am. Chem. Soc.* **2008**, *130*, 3959–3966.
- (10) Wasmer, C.; Lange, A.; Van Melckebeke, H.; Siemer, A. B.; Riek, R.; Meier, B. H. *Science* **2008**, *319*, 1523–1526.
- (11) Bertini, I.; Bhaumik, A.; De Paepe, G.; Griffin, R. G.; Lelli, M.; Lewandowski, J. R.; Luchinat, C. *J. Am. Chem. Soc.* **2010**, *132*, 1032–1040.
- (12) Cady, S. D.; Schmidt-Rohr, K.; Wang, J.; Soto, C. S.; DeGrado, W. F.; Hong, M. *Nature* **2010**, *463*, 689–693.
- (13) Jehle, S.; Rajagopal, P.; Bardiaux, B.; Markovic, S.; Kuhne, R.; Stout, J. R.; Higman, V. A.; Kleivit, R. E.; van Rossum, B. J.; Oschkinat, H. *Nat. Struct. Mol. Biol.* **2010**, *17*, 1037–1042.
- (14) Zhang, Y.; Doherty, T.; Li, J.; Lu, W. Y.; Barinka, C.; Lubkowski, J.; Hong, M. *J. Mol. Biol.* **2010**, *397*, 408–422.
- (15) Linser, R.; Bardiaux, B.; Higman, V.; Fink, U.; Reif, B. *J. Am. Chem. Soc.* **2011**, *133*, 5905–5912.
- (16) Tang, M.; Sperling, L. J.; Berthold, D. A.; Schwieters, C. D.; Nesbitt, A. E.; Nieuwkoop, A. J.; Gennis, R. B.; Rienstra, C. M. *J. Biomol. NMR* **2011**, *51*, 227–233.
- (17) Wylie, B. J.; Sperling, L. J.; Nieuwkoop, A. J.; Franks, W. T.; Oldfield, E.; Rienstra, C. M. *Proc. Natl. Acad. Sci. U.S.A.* **2011**, *108*, 16974–16979.
- (18) Knight, M. J.; Pell, A. J.; Bertini, I.; Felli, I. C.; Gonnelli, L.; Pierattelli, R.; Herrmann, T.; Emsley, L.; Pintacuda, G. *Proc. Natl. Acad. Sci. U.S.A.* **2012**, *109*, 11095–11100.
- (19) Loquet, A.; Sgourakis, N. G.; Gupta, R.; Giller, K.; Riedel, D.; Goosmann, C.; Griesinger, C.; Kolbe, M.; Baker, D.; Becker, S.; Lange, A. *Nature* **2012**, *486*, 276–279.
- (20) Etzkorn, M.; Martell, S.; Andronesi, O. C.; Seidel, K.; Engelhard, M.; Baldus, M. *Angew. Chem., Int. Ed.* **2007**, *46*, 459–462.
- (21) Shi, L. C.; Kawamura, I.; Jung, K. H.; Brown, L. S.; Ladizhansky, V. *Angew. Chem., Int. Ed.* **2011**, *50*, 1302–1305.
- (22) Shi, L. C.; Lake, E. M. R.; Ahmed, M. A. M.; Brown, L. S.; Ladizhansky, V. *Biochim. Biophys. Acta, Biomembr.* **2009**, *1788*, 2563–2574.
- (23) Suter, D.; Ernst, R. R. *Phys. Rev. B* **1985**, *32*, 5608–5627.
- (24) Takegoshi, K.; Nakamura, S.; Terao, T. *Chem. Phys. Lett.* **2001**, *344*, 631–637.
- (25) Lange, A.; Luca, S.; Baldus, M. *J. Am. Chem. Soc.* **2002**, *124*, 9704–9705.
- (26) Michal, C. A.; Jelinski, L. W. *J. Am. Chem. Soc.* **1997**, *119*, 9059–9060.
- (27) Jaroniec, C. P.; Filip, C.; Griffin, R. G. *J. Am. Chem. Soc.* **2002**, *124*, 10728–10742.
- (28) De Paepe, G.; Lewandowski, J. R.; Loquet, A.; Eddy, M.; Megy, S.; Bockmann, A.; Griffin, R. G. *J. Chem. Phys.* **2011**, *134*, 095101–095118.
- (29) Bertini, I.; Luchinat, C.; Parigi, G.; Pierattelli, R. *ChemBioChem* **2005**, *6*, 1536–1549.
- (30) Otting, G. *J. Biomol. NMR* **2008**, *42*, 1–9.
- (31) Bertini, I.; Luchinat, C.; Parigi, G. *Prog. Nucl. Magn. Reson. Spectrosc.* **2002**, *40*, 249–273.
- (32) Jovanovic, T.; McDermott, A. E. *J. Am. Chem. Soc.* **2005**, *127*, 13816–13821.
- (33) Balayssac, S.; Bertini, I.; Lelli, M.; Luchinat, C.; Maletta, M. *J. Am. Chem. Soc.* **2007**, *129*, 2218–2219.
- (34) Nadaud, P. S.; Helmus, J. J.; Hofer, N.; Jaroniec, C. P. *J. Am. Chem. Soc.* **2007**, *129*, 7502–7503.
- (35) Wickramasinghe, N. P.; Kotecha, M.; Samoson, A.; Past, J.; Ishii, Y. *J. Magn. Reson.* **2007**, *184*, 350–356.
- (36) Balayssac, S.; Bertini, I.; Bhaumik, A.; Lelli, M.; Luchinat, C. *Proc. Natl. Acad. Sci. U.S.A.* **2008**, *105*, 17284–17289.
- (37) Linser, R.; Fink, U.; Reif, B. *J. Am. Chem. Soc.* **2009**, *131*, 13703–13708.
- (38) Nadaud, P. S.; Helmus, J. J.; Kall, S. L.; Jaroniec, C. P. *J. Am. Chem. Soc.* **2009**, *131*, 8108–8120.
- (39) Bertini, I.; Emsley, L.; Lelli, M.; Luchinat, C.; Mao, J. F.; Pintacuda, G. *J. Am. Chem. Soc.* **2010**, *132*, 5558–5559.
- (40) Tang, M.; Berthold, D. A.; Rienstra, C. M. *J. Phys. Chem. Lett.* **2011**, *2*, 1836–1841.
- (41) Su, Y. C.; Hu, F. H.; Hong, M. *J. Am. Chem. Soc.* **2012**, *134*, 8693–8702.
- (42) Luchinat, C.; Parigi, G.; Ravera, E.; Rinaldelli, M. *J. Am. Chem. Soc.* **2012**, *134*, 5006–5009.
- (43) Nadaud, P. S.; Helmus, J. J.; Sengupta, I.; Jaroniec, C. P. *J. Am. Chem. Soc.* **2010**, *132*, 9561–9563.
- (44) Linser, R.; Chevelkov, V.; Diehl, A.; Reif, B. *J. Magn. Reson.* **2007**, *189*, 209–216.
- (45) Wickramasinghe, N. P.; Parthasarathy, S.; Jones, C. R.; Bhardwaj, C.; Long, F.; Kotecha, M.; Mehboob, S.; Fung, L. W. M.; Past, J.; Samoson, A.; Ishii, Y. *Nat. Methods* **2009**, *6*, 215–218.
- (46) Su, Y.; Mani, R.; Hong, M. *J. Am. Chem. Soc.* **2008**, *130*, 8856–8864.
- (47) Knight, M. J.; Felli, I. C.; Pierattelli, R.; Bertini, I.; Emsley, L.; Herrmann, T.; Pintacuda, G. *J. Am. Chem. Soc.* **2012**, *134*, 14730–14733.
- (48) Sengupta, I.; Nadaud, P. S.; Helmus, J. J.; Schwieters, C. D.; Jaroniec, C. P. *Nat. Chem.* **2012**, *4*, 410–417.
- (49) Wang, S. L.; Munro, R. A.; Kim, S. Y.; Jung, K. H.; Brown, L. S.; Ladizhansky, V. *J. Am. Chem. Soc.* **2012**, *134*, 16995–16998.

- (50) Knight, M.; Felli, I. C.; Pierattelli, R.; Emsley, L.; Pintacuda, G. *Acc. Chem. Res.* **2013**, in press, DOI: 10.1021/ar300349y.
- (51) Jaroniec, C. P. *Solid State Nucl. Magn. Reson.* **2012**, 43–44, 1–13.
- (52) Su, X. C.; Man, B.; Beeren, S.; Liang, H.; Simonsen, S.; Schmitz, C.; Huber, T.; Messerle, B. A.; Otting, G. *J. Am. Chem. Soc.* **2008**, 130, 10486–10487.
- (53) Franks, W. T.; Zhou, D. H.; Wylie, B. J.; Money, B. G.; Graesser, D. T.; Frericks, H. L.; Sahota, G.; Rienstra, C. M. *J. Am. Chem. Soc.* **2005**, 127, 12291–12305.
- (54) Das, R.; Baker, D. *Annu. Rev. Biochem.* **2008**, 77, 363–382.
- (55) Schmitz, C.; Vernon, R.; Otting, G.; Baker, D.; Huber, T. *J. Mol. Biol.* **2012**, 416, 668–677.
- (56) Shen, Y.; Lange, O.; Delaglio, F.; Rossi, P.; Aramini, J. M.; Liu, G. H.; Eletsky, A.; Wu, Y. B.; Singarapu, K. K.; Lemak, A.; Ignatchenko, A.; Arrowsmith, C. H.; Szyperski, T.; Montelione, G. T.; Baker, D.; Bax, A. *Proc. Natl. Acad. Sci. U.S.A.* **2008**, 105, 4685–4690.
- (57) Neue, G.; Dybowski, C. *Solid State Nucl. Magn. Reson.* **1997**, 7, 333–336.
- (58) Morcombe, C. R.; Zilm, K. W. *J. Magn. Reson.* **2003**, 162, 479–486.
- (59) Baldus, M.; Petkova, A. T.; Herzfeld, J.; Griffin, R. G. *Mol. Phys.* **1998**, 95, 1197–1207.
- (60) Delaglio, F.; Grzesiek, S.; Vuister, G. W.; Zhu, G.; Pfeifer, J.; Bax, A. *J. Biomol. NMR* **1995**, 6, 277–293.
- (61) Allegrozzi, M.; Bertini, I.; Janik, M. B. L.; Lee, Y. M.; Lin, G. H.; Luchinat, C. *J. Am. Chem. Soc.* **2000**, 122, 4154–4161.
- (62) Su, X. C.; Otting, G. *J. Biomol. NMR* **2010**, 46, 101–112.
- (63) Loquet, A.; Lv, G.; Giller, K.; Becker, S.; Lange, A. *J. Am. Chem. Soc.* **2011**, 133, 4722–4725.
- (64) Schmitz, C.; Stanton-Cook, M. J.; Su, X. C.; Otting, G.; Huber, T. *J. Biomol. NMR* **2008**, 41, 179–189.